JOURNAL OF Materials CHEMISTRY

Electrochemical, electrical and magnetic properties and valence state distributions in the high voltage spinel cathode solid solutions $Li_{1-X}Co_{1/2+3X/2}Mn_{3/2-X/2}O_4$: $-0.33 \leqslant X \leqslant 1$

Anthony R. West,*[a] Hiroo Kawai,[a] Hiroyuki Kageyama,[b] Mitsuharu Tabuchi,[b] Mikito Nagata[c] and Hisashi Tukamoto[c]

[a]*Department of Engineering Materials, University of Sheffield, Mappin Street, Sheffield, UK S1 3JD*
[b]*Osaka National Research Institute, 1-8-31 Midorigaoka, Ikeda, Osaka 563, Japan*
[c]*Corporate R&D Centre, Japan Storage Battery Company Limited, Nishinosho, Kisshoin, Minami-ku, Kyoto 601, Japan*

Received 26th February 2001, Accepted 15th March 2001
First published as an Advance Article on the web 23rd April 2001

An extensive series of spinel solid solutions covering most of the range between $Li_4Mn_5O_{12}$ and Co_2MnO_4 including $Li_2CoMn_3O_8$, (or $LiCo_{1/2}Mn_{3/2}O_4$) and with the general formula, $Li_{1-X}Co_{1/2+3X/2}Mn_{3/2-X/2}O_4$: $-0.17 \leqslant X \leqslant 0.84$, forms in air at 800 °C with a final heating at 600 °C. From the combined data of powder X-ray diffraction (XRD) and X-ray absorption near edge spectroscopy (XANES), the solid solutions have the structural formulae $[Li^+]_{8a}[Li^+_{1-X}Co^{3+}_{1/2+3X/2}Mn^{3+}_{1/2+3X/2}Mn^{4+}_{1-2X}]_{16d}O_4$ for $X \leqslant 0$ and $[Li^+_{1-X}Co^{2+}_X]_{8a}[Co^{3+}_{1/2+X/2}Mn^{3+}_{1/2+X/2}Mn^{4+}_{1-X}]_{16d}O_4$ for $X \geqslant 0$, in space group $Fd\bar{3}m$; 1 : 3 ordering of cations on octahedral 16*d* sites may occur for compositions around $X = 0$, but was not detected by XRD. Observed effective magnetic moment values from magnetic susceptibility data are consistent with these formulae. Weiss temperatures become increasingly negative with increasing X, with evidence for spontaneous magnetisation below *ca.* 150 K, suggesting the presence of ferromagnetic interaction between Co^{2+} and Mn^{3+} or Mn^{4+} for samples with $X > 0$. Impedance data on pellets with blocking electrodes demonstrate a modest level of semiconductivity which may involve mainly Mn^{3+}/Mn^{4+} situated in adjacent octahedral 16*d* sites. Potential profiles for electrochemical cells, $Li/Li_{1-X}Co_{1/2+3X/2}Mn_{3/2-X/2}O_4$: $-0.17 \leqslant X \leqslant 0.18$, reveal a charge/discharge plateau centred on *ca.* 4.0 V, and a second plateau centred on *ca.* 5.1 V which shows a maximum discharge capacity of *ca.* 62 mA h g^{-1} at $X = 0$, *i.e.*, $Li_2CoMn_3O_8$. For $X \gg 0$, the solid solutions lose their electrochemical activity as a cathode possibly because the Co that resides in tetrahedral 8*a* sites blocks Li^+ conduction through the pathway: tetrahedral 8*a* site–empty octahedral 16*c* site. For $X < 0$, the first charging cycle is not reproduced on subsequent discharge/charge cycles; reasons for this are not understood. In order to explain the large capacities of charge/discharge for $X < 0$, some additional redox process, possibly O^{2-}/O^-, appears to be necessary.

Introduction

Intense investigations[1] into cathode materials for lithium ion rechargeable batteries have been made for the last two decades, leading to the recent commercialisation[2,3] of 4 V cells with cathodes, $LiCoO_2$[4] and $LiMn_2O_4$.[5–7] These cells are used in portable electronic devices,[8] but larger scale batteries for zero emission vehicles require improved energy density which is attained by either increasing the capacity or raising the operating voltage. Lithium cathode materials that exhibit larger capacity include $LiMnO_2$[9,10] and $Li_{1.5}Na_{0.5}MnO_{2.85}I_{0.12}$,[11] but the former needs improved cycling stability and the latter requires higher working voltage and a less inclined discharge plateau.

Improved electrolytes[12,13] have recently made it possible to explore the potential range to *ca.* 5 V *vs.* Li/Li^+. All high-voltage lithium cathode materials[14] reported so far that operate over 4.5 V are complex spinel-structure oxides based on $Li_2MM'_3O_8$ and $LiMM'O_4$: $MM'_3 = CrMn_3$,[15,16] $FeMn_3$,[17] $CoMn_3$,[18] $NiMn_3$,[19,20] $CuMn_3$;[21,22] $MM' = CrMn$,[15,16] $CoMn$,[23] NiV.[24] Spinels $Li_2MM'_3O_8$ and $LiMM'O_4$ may exhibit cation order on the octahedral sites, *i.e.*, 1 : 3 order for many $Li_2MM'_3O_8$ spinels[25,26] and 1 : 1 order for several $LiMM'O_4$ spinels.[27,28] Thus, they may be regarded as separate phases, distinct from simple binary spinels such as $LiMn_2O_4$ and solid solutions derived from these, which do not show such cation order.[14]

The first cathode materials reported to operate at discharge voltage above 5 V are $Li_2CoMn_3O_8$[18] and $LiCoMnO_4$.[23] There exists a potentially large family of spinel-structure oxides in the system Li–Co–Mn–O which includes two spinel compositional series with cation to anion ratio of 3 : 4, Fig. 1. One series is between the two binary spinels $LiMn_2O_4$[5–7] and $LiCo_2O_4$:[29] a spinel solid solution of general formula $Li_2Co_{1+Y}Mn_{3-Y}O_8$ forms, at least in the range $-1 \leqslant Y \leqslant 1$, in air at 600 °C and includes the two above-mentioned phases $Li_2CoMn_3O_8$ ($Y = 0$) and $LiCoMnO_4$ ($Y = 1$).[23,30] Potential profiles recorded for electrochemical cells containing these spinels as the cathode exhibited a clear plateau centred on *ca.* 5.0 V for $Y \geqslant -0.6$, which showed a maximum discharge capacity of *ca.* 95 mA h g^{-1} at $Y = 0.6$ and 1.0.[23,30] As a result, these two cathodes show superior energy density to $LiMn_2O_4$, the cathode material used in state-of-the-art cells.[23,30]

The other simple series is between the two binary spinels $Li_4Mn_5O_{12}$[31,32] and Co_2MnO_4:[33] this series may be written as $Li_{1-X}Co_{1/2+3X/2}Mn_{3/2-X/2}O_4$, and includes $Li_2CoMn_3O_8$ at $X = 0$. Here we survey the formation of spinel solid solutions in this series over the range $-0.33 \leqslant X \leqslant 1$, in air at 600 °C, and discuss the cation and charge distributions, as determined by a combination of X-ray Rietveld refinement and XANES

 DOI: 10.1039/b101788h

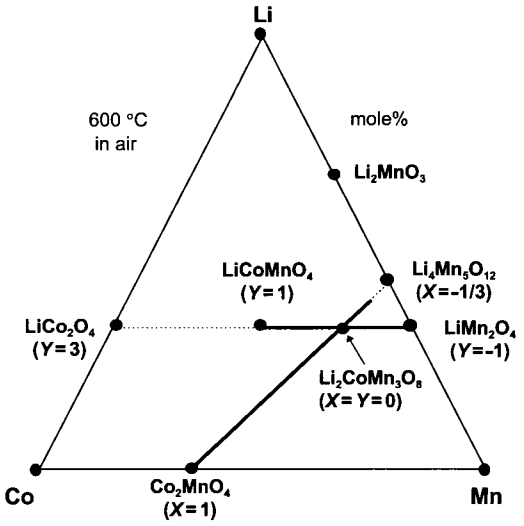

Fig. 1 Formation of $Li_{1-X}Co_{1/2+3X/2}Mn_{3/2-X/2}O_4$ and $LiCo_{1/2+Y/2}Mn_{3/2-Y/2}O_4$ (thick lines) spinel solid solutions in the system Li–Co–Mn–O. Oxygen contents are not specified.

spectroscopy, together with electrical, magnetic and electrochemical property measurements.

Experimental

Stoichiometric mixtures of dried starting materials Li_2CO_3, CoO and $MnCO_3$, all reagent grade, were ground intimately, fired in air, initially at 650 °C for 2 h to decarbonate then at 800 °C for 3 days with intermittent regrinding and finally at 600 °C for 3 days, followed by quenching to room temperature.

Powder X-ray diffraction was performed with a Stoe Stadi/P diffractometer, Cu-Kα_1 radiation, using Si as an external standard: a scan range of $8° < 2\theta < 113°$ in steps of 0.2° was used for Rietveld refinement. The data were analysed using the Stoe software package: lattice parameter refinement was carried out with the LATREF program and Rietveld refinement with the pattern fitting structure refinement (PFSR) program.

X-Ray absorption spectra were recorded in transmission mode on an EXAC-820 spectrometer, using a Ge(400) monochromator. Co K-edge XANES used $Li_2CoGe_3O_8$ and $LiCoO_2$ as references: $Li_2CoGe_3O_8$ contains Co^{2+} essentially in tetrahedral sites,[26] and $LiCoO_2$ contains Co^{3+} in octahedral sites. Mn K-edge XANES used Mn_2O_3, $LiMn_2O_4$ and $Li_2MgMn_3O_8$ as references: these contain Mn in octahedral sites, with average valence states of 3+, 3.5+ and 4+, respectively.[30]

Magnetic measurements were performed in He between 83 and 520 K using a MB-3 Shimazu Faraday balance with Tutton's salt, $(NH_4)_2Mn(SO_4)_2{\cdot}6H_2O$, to calibrate the magnetization data.

For conductivity measurements, the as-prepared samples were cold-pressed to form pellets (8 mm diameter; 2–3 mm thickness), which were then sintered at 950 °C for a few hours in order to increase the mechanical strength, slowly cooled to 600 °C and maintained at 600 °C for 3 days, before quenching to room temperature. In/Ga paste electrodes were coated on opposite sides of the sintered pellets. Impedance data over the temperature range −40 °C to 30 °C were recorded with Hewlett–Packard 4192 instrumentation, and analysed in three formalisms,[34] the complex impedance (Z^*), admittance (Y^*), and modulus (M^*), using in-house software.

To make positive electrodes for electrochemical testing, the samples were blended with 5 wt% acetylene black and 8 wt% polyvinylidene fluoride binder. Electrochemical measurements used a glass test cell containing the above composite positive electrode, Li metal foil as the negative electrode, Li metal as a reference and 1 M $LiPF_6$ dissolved in propylene carbonate as the electrolyte. Cycle tests were performed galvanostatically in the range 3.0–5.3 V *vs.* Li/Li^+, using, unless noted, a current density of 0.5 mA cm^{-2}.

Results

Powder XRD indicated that, after reaction at 800 °C followed by a post-reaction anneal at 600 °C, a range of spinel solid solutions of general formula $Li_{1-X}Co_{1/2+3X/2}Mn_{3/2-X/2}O_4$ formed over the range $-0.17 \leqslant X \leqslant 1$. Small amounts of Li_2MnO_3 were detected in compositions with $X < -0.17$, consistent with the reported difficulty in synthesis of pure $Li_4Mn_5O_{12}$, $X = -0.33$.[35] These compositions containing $X < -0.17$ have not been studied further here.

Powder XRD patterns of all the spinel solid solutions in the range $-0.17 \leqslant X \leqslant 1$ were indexed in the cubic space group $Fd\bar{3}m$. Lattice parameters, a, as a function of composition are shown in Fig. 2; they pass through a minimum at $X = 0$ and increase to either side, thus indicating that compositions to either side of $X = 0$ have distinctly different solid solution mechanisms. In the range $X \leqslant 0$, a increases linearly until the limit of the phase-pure region, *i.e.*, $X \sim -0.20$; in the range $X \geqslant 0$, a increases linearly until $X \sim 0.84$, after which, apparent deviation from linearity takes place. Compositions at $X \geqslant 0.8$ have not been studied further; possibly the Co : Mn ratio departs from 2 : 1, or oxygen loss occurs.

Structural and valence state characterisation

We reported previously, using Rietveld refinement of powder XRD data, that $Li_2CoMn_3O_8$ has the cation distribution $[Li]_{8a}[Co_{0.5}Mn_{1.5}]_{16d}O_4$: all Li is located in tetrahedral 8*a* sites; Co and Mn in 1 : 3 ratio are distributed over octahedral 16*d* sites.[18] Cation order[25,26] on the octahedral sites is possible, since although XRD data revealed no evidence of superstructure reflections, Co and Mn have very similar atomic scattering factors.[18]

In the present study, structure refinement was carried out for compositions to either side of $X = 0$, at $X = -0.173$ and 0.381, using the starting atomic positions of the spinel phase, $Li_4Mn_5O_{12}$,[31] with initial isotropic thermal parameters, 0.05 $Å^3$, for all atomic positions. Theoretical XRD patterns were generated initially for various models with different cation distributions on 8*a* and 16*d* sites. This demonstrated that Co and Mn preferentially occupied octahedral 16*d* sites for both

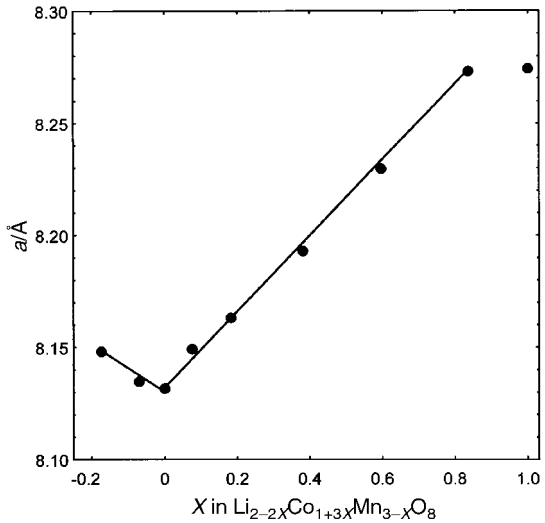

Fig. 2 Variation in lattice parameter, a, with composition, X, for spinel solid solutions $Li_{1-X}Co_{1/2+3X/2}Mn_{3/2-X/2}O_4$.

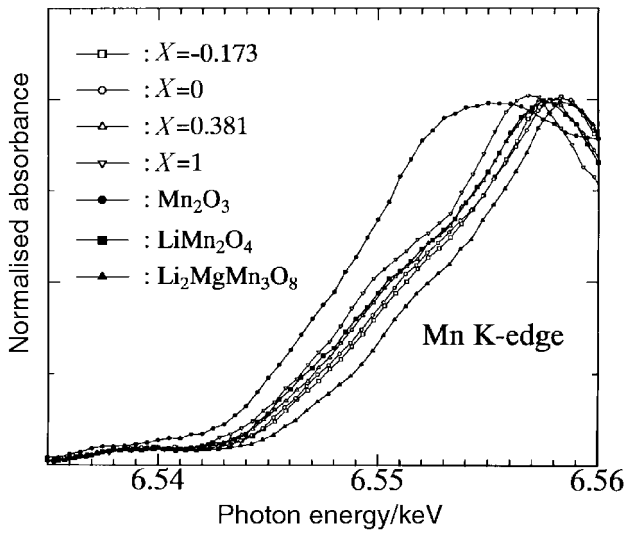

Fig. 3 Mn K-edge XANES spectra; Mn_2O_3, $LiMn_2O_4$ and $Li_2MgMn_3O_8$ are used as references.

samples. Mn K-edge XANES spectra for $X=-0.173$, 0 and 0.381 resembled one another, Fig. 3. This indicates that Mn in all three samples is surrounded similarly by oxygen, and thus $X=-0.173$ and 0.381 are also likely to have all Mn in octahedral sites. The Co K-edge absorption spectrum for $X=-0.173$, Fig. 4, resembles that of $X=0$, and thus $X=-0.173$ is also likely to have all Co in octahedral sites; the Co K-edge absorption spectrum for $X=0.381$ is shifted significantly, however, which could be consistent with the presence of some Co in tetrahedral sites.

The Mn K-edge XANES spectrum for $Li_2CoMn_3O_8$, $X=0$, has the overall position of its absorption edge between those of $Li_2MgMn_3O_8$ and $LiMn_2O_4$, Fig. 3; the average valence state of Mn in $Li_2CoMn_3O_8$ is therefore estimated to be between 3.5+ and 4+. The Co K-edge XANES spectrum for $Li_2CoMn_3O_8$, Fig. 4, has threshold energy very similar to that of $LiCoO_2$, and thus Co in $Li_2CoMn_3O_8$ appears to have valence state 3+. Consequently, Rietveld refinement fixed Mn at 16*d* sites, and allowed the exchange of Co with Li over 8*a* and 16*d* sites. *R* values[36] were used to evaluate the refinement results. Results are summarised in Tables 1 and 2.

$Li_{1.17}Co_{0.24}Mn_{1.59}O_4$ ($X=-0.173$) was found to have the cation distribution $[Li]_{8a}[Li_{0.17}Co_{0.24}Mn_{1.59}]_{16d}O_4$: Li fully occupies tetrahedral 8*a* sites; octahedral 16*d* sites contain Li, Co and Mn. $LiCo_{1/2}Mn_{3/2}O_4$ ($X=0$) has the distribution $[Li]_{8a}[Co_{0.5}Mn_{1.5}]_{16d}O_4$. $Li_{0.62}Co_{1.07}Mn_{1.31}O_4$ ($X=0.381$) has the distribution $[Li_{0.62}Co_{0.38}]_{8a}[Co_{0.69}Mn_{1.31}]_{16d}O_4$: Li and Co are randomly distributed over the tetrahedral 8*a* sites whereas the octahedral 16*d* sites are occupied by Co and Mn.

Table 1 Structure refinement parameters for $Li_{2.34}Co_{0.48}Mn_{3.18}O_8$ ($X=-0.173$)

Atom	Site	*x*/*a*	*y*/*b*	*z*/*c*	U_{iso}/Å^3	Occupancy
Li(1)	8*a*	0.125	0.125	0.125	0.02(3)	1
Li(2)	16*d*	0.5	0.5	0.5	0.05	0.085
Co	16*d*	0.5	0.5	0.5	0.05	0.120
Mn	16*d*	0.5	0.5	0.5	0.01(1)	0.795
O	32*e*	0.2584(9)	0.2584(9)	0.2584(9)	0.020(5)	1

Space group $Fd\bar{3}m$; $a=8.1481(9)$ Å; $R_p=1.61\%$; $R_{wp}=2.07\%$.

Table 2 Structure refinement parameters for $Li_{1.24}Co_{2.14}Mn_{2.62}O_8$ ($X=0.381$)

Atom	Site	*x*/*a*	*y*/*b*	*z*/*c*	U_{iso}/Å^3	Occupancy
Li	8*a*	0.125	0.125	0.125	0.012(14)	0.62
Co(1)	8*a*	0.125	0.125	0.125	0.012(14)	0.38
Co(2)	16*d*	0.5	0.5	0.5	0.017(6)	0.345
Mn	16*d*	0.5	0.5	0.5	0.017(6)	0.655
O	32*e*	0.254(2)	0.254(2)	0.254(2)	0.040(12)	1

Space group $Fd\bar{3}m$; $a=8.1929(15)$ Å; $R_p=2.01\%$; $R_{wp}=2.55\%$.

The Mn K-edge absorption spectrum for $X=-0.173$ is at slightly higher energy than that of $X=0$, Fig. 3. The increase occurs in spite of an increase in lattice parameter, Fig. 2, and clearly indicates that the valence state of Mn for $X=-0.173$ is higher than that of $X=0$.[30] This increase in threshold energy is probably due to an increase in metal–ligand bond strength associated with an increased oxidation state of the cation. By contrast, the Co K-edge absorption spectrum for $X=-0.173$ is at slightly lower energy than that of $X=0$, Fig. 4. This decrease can be explained by the increase in lattice parameter, Fig. 2, without the necessity of involving any change in oxidation state of Co. These XANES results, together with the XRD refinements, lead us to conclude that $Li_{1.17}Co_{0.24}Mn_{1.59}O_4$ ($X=-0.173$) has the structural formula $[Li^+]_{8a}[Li^+_{0.17}Co^{3+}_{0.24}Mn^{3+}_{0.24}Mn^{4+}_{1.35}]_{16d}O_4$ whereas $X=0$ has the structural formula $[Li^+]_{8a}[Co^{3+}_{0.5}Mn^{3+}_{0.5}Mn^{4+}]_{16d}O_4$.

The Mn K-edge absorption spectrum for $X=0.381$ is at somewhat lower energy than that of $X=0$, Fig. 3. This decrease

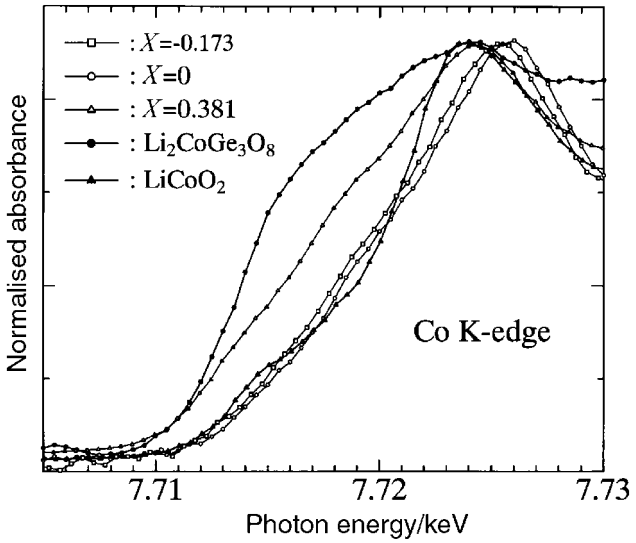

Fig. 4 Co K-edge XANES spectra; $Li_2CoGe_3O_8$ and $LiCoO_2$ are used as references.

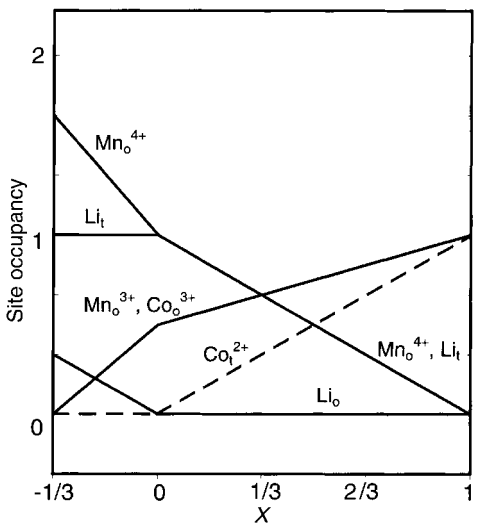

Fig. 5 Change in occupancy of tetrahedral 8*a* (t) and octahedral 16*d* (o) sites with composition *X*.

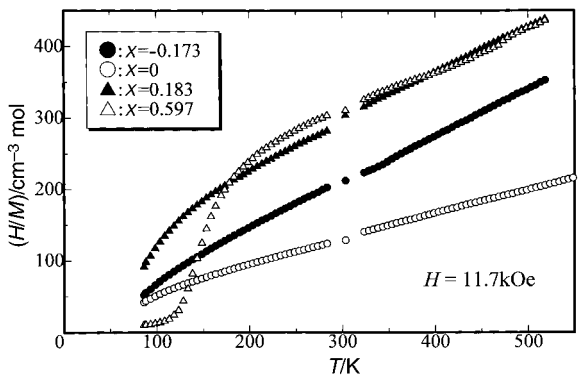

Fig. 6 Temperature dependence of the inverse molar magnetisation.

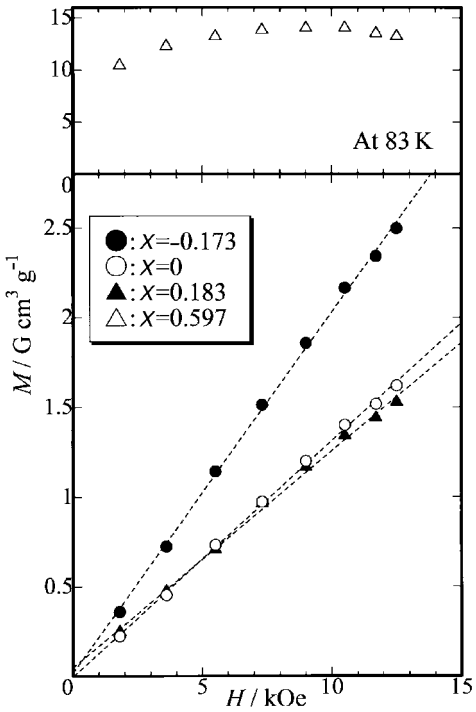

Fig. 7 Field dependence of the magnetisation at 83 K.

is attributable partly to an increase in lattice parameter, Fig. 2, and partly to a decrease in oxidation state of Mn. The corresponding Co K-edge is shifted to much lower energy than that for $X=0$, Fig. 4, and thus Co in $X=0.381$ probably exhibits a mixed valence state between 2+ and 3+. Since the XRD refinement shows that Co occupies both tetrahedral and octahedral sites, then by taking account of crystal field stabilisation,[37] it is reasonable to assume that Co^{3+} occupies octahedral sites and Co^{2+} is in the tetrahedral sites. These XANES results together with the XRD refinements lead to the structural formula $[Li^{+}_{0.62}Co^{2+}_{0.38}]_{8a}[Co^{3+}_{0.69}Mn^{3+}_{0.69}Mn^{4+}_{0.62}]_{16d}O_4$ for $X=0.381$.

The linear change in a with X for $-0.173 \leqslant X \leqslant 0$ and the structural formulae determined for $X=-0.173$ and 0 lead to the general formula $[Li^{+}]_{8a}[Li^{+}_{-X}Co^{3+}_{1/2+3X/2}Mn^{3+}_{1/2-3X/2}Mn^{4+}_{1-2X}]_{16d}O_4$ for $-0.173 \leqslant X \leqslant 0$. This is based on the substitution mechanism $3/2Co^{3+}_{16d}+3/2Mn^{3+}_{16d}=2Mn^{4+}_{16d}+Li^{+}_{16d}$, and leads to the well-established formula $[Li^{+}]_{8a}[Li^{+}_{0.33}Mn^{4+}_{1.67}]_{16d}O_4$[31,32] at the limiting composition $X=-0.33$, *i.e.* $Li_4Mn_5O_{12}$. This end-member phase, $Li_4Mn_5O_{12}$, is not stable at high temperatures, which explains why, in our samples heated at 600 °C, the spinel solid solutions did not extend as far as this composition.

The linear change in a with X for $0 \leqslant X \leqslant 0.84$ and the structural formulae determined for $X=0$ and 0.381 lead to the general formula $[Li^{+}_{1-X}Co^{2+}_{X}]_{8a}[Co^{3+}_{1/2+X/2}Mn^{3+}_{1/2+X/2}Mn^{4+}_{1-X}]_{16d}O_4$ for $0 \leqslant X \leqslant 0.84$ which is based on the mechanism $Li^{+}_{8a}+Mn^{4+}_{16d}=Co^{2+}_{8a}+1/2Co^{3+}_{16d}+1/2Mn^{3+}_{16d}$, and extrapolates to the expected formula $[Co^{2+}]_{8a}[Co^{3+}Mn^{3+}]_{16d}O_4$[33] at $X=1$.

XANES spectra in the range $0 \leqslant X \leqslant 0.84$ supported the above formula: thus, (1) Mn and Co K-edge absorption spectra each shifted to lower energy with X, and therefore, the oxidation states of Mn and Co are both likely to decrease with X; (2) all samples had similar-shaped Mn K-edge spectra and are therefore likely to contain Mn in only octahedral sites; (3) the Co K-edge spectra shifted significantly with X; consequently the concentration of Co in tetrahedral sites increases with X.

From these various results, a model for the change in site occupancy of tetrahedral and octahedral sites with composition is obtained and presented in Fig. 5. With increasing X: Mn^{4+} and Li^{+} in octahedral sites are replaced by a mixture of Mn^{3+} and Co^{3+}; Li^{+} in tetrahedral sites is gradually replaced by Co^{2+}, but only for $X \geqslant 0$. The decrease in lattice parameter with X over the range $-0.17 \leqslant X \leqslant 0$ is attributed to the net effect of replacing Li on octahedral sites by Mn^{3+}/Co^{3+}. The increase in lattice parameter over the range $0 \leqslant X \leqslant 0.84$ is attributed to the replacement of Mn^{4+} on octahedral sites by a mixture of Mn^{3+} and Co^{3+}. This more than offsets the effect of substituting Li on tetrahedral sites by Co^{2+}.

Magnetic properties

The temperature dependence of the inverse molar magnetisation normalized by magnetic field (H/M) is shown in Fig. 6. The field dependence of the magnetisation at 83 K is shown in Fig. 7. No spontaneous magnetization was observed at 300 K for any sample, indicating that H/M could be considered as the inverse molar susceptibility. Magnetic properties extracted from these plots are summarised in Table 3.

Curie–Weiss paramagnetic behaviour was observed for all samples and therefore, the effective magnetic moment (μ_{eff}) and Weiss temperature (θ) values were calculated from (H/M)–T plots above 300 K. Deviation from Curie–Weiss paramagnetic behaviour below 200 K was observed for the samples with positive X values due to spontaneous magnetization originating from magnetic order between Co^{2+} and Mn ions; for $X=1$, the

Table 3 Magnetic parameters for Co-doped lithium manganese spinels

X Value	Cation distribution[a]	μ_{eff}/μ_B	μ_{eff}/μ_B[b] Calc.	θ/K	M_g/G cm^3 g^{-1} (at 83 K)
−0.173	$(Li)_{8a}[Li_{0.17}Co_{0.24}Mn_{1.59}]_{16d}O_4$	4.683(7)	5.11	−12	0.02(3)
0	$(Li)_{8a}[Co_{0.5}Mn_{1.5}]_{16d}O_4$	4.793(9)	5.20	−76	0.00(2)
0.183	$(Li_{0.815}Co_{0.185})_{8a}[Co_{0.589}Mn_{1.411}]_{16d}O_4$	5.111(12)	5.41	−142	0.05(2)
0.597	$(Li_{0.402}Co_{0.597})_{8a}[Co_{0.799}Mn_{1.201}]_{16d}0_4$	6.04(3)	5.84	−242	12.5(6)

[a]Cation distributions determined by X-ray Rietveld analysis and XANES spectra. [b]Calculated effective magnetic moment values were obtained by assuming that Co ions on 8*a* and 16*d* sites are high-spin 2+ ($S=3/2$) and low spin 3+ ($S=0$) states, respectively and that Mn ions are mixed valence state of high-spin 3+ ($S=2$) and 4+ ($S=3/2$) states; previous data on end-member compositions showed the cation distributions of $LiMn_2O_4$ and Co_2MnO_4 are $(Li)_{8a}$[high-spin $Mn^{3+}Mn^{4+}]_{16d}O_4$ and (high-spin $Co^{2+})_{8a}$[low-spin Co^{3+}high-spin $Mn^{3+}]_{16d}O_4$, respectively.

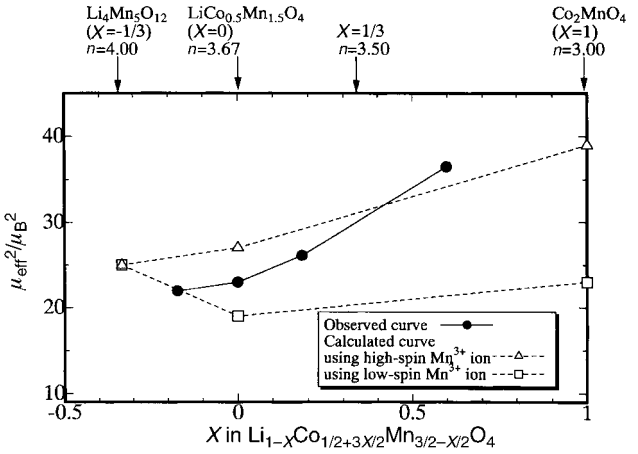

Fig. 8 Relation between the square of the paramagnetic moment per chemical formula normalized by the Bohr magneton, $(\mu_{eff}/\mu_B)^2$ and X. n is the average valence state of Mn.

Curie temperature has been reported to be 170–180 K for ferrimagnetic Co_2MnO_4.[33] Thus, the appearance of antiferromagnetic interaction between Co^{2+} and Mn ions is supported by the change in Weiss temperature to large negative values with increasing X for $X>0$. The large negative value for the sample with $X=0$ compared to that for $X=-0.173$ can be explained by the suppression of ferromagnetic interaction between adjacent Mn^{4+} ions on 16d sites due to the occurrence of antiferromagnetic Mn^{3+}–Mn^{4+} interaction. This suggestion arises from a similar comparison between θ values for $Li_4Mn_5O_{12}$ (+40 K)[34] and $LiMn_2O_4$ (−266 K)[38].

On comparing experimental and calculated μ_{eff} values and their variation with X, Table 3, a large disagreement is observed for three samples with $X<0.2$. Since these samples can be considered as manganese-rich, with Mn/(Co+Mn) $\geqslant 0.73$, we consider that the change in μ_{eff} with X is mainly governed by the electronic configuration of Mn^{3+} and Mn^{4+} ions on octahedral 16d sites. Using the chemical formula derived from analysis of XRD and XANES data, the calculated compositional dependence of μ_{eff}^2 was obtained for $-1/3 \leqslant X \leqslant 0$ from the sum of the magnetic susceptibility of each magnetic ion, as follows:

$$(\mu_{eff}/\mu_B)^2 = (1/2+3/2X)\mu^2_{Co^{3+}} + (1/2+3/2X)\mu^2_{Mn^{3+}} + (1-2X)\mu^2_{Mn^{4+}} \quad (1)$$

in which $\mu_{Co^{3+}}$, $\mu_{Mn^{3+}}$ and $\mu_{Mn^{4+}}$ are the spin-only paramagnetic moments of low-spin Co^{3+}, Mn^{3+} and Mn^{4+} ions, respectively. If all Mn^{3+} ions are in the high spin ($S=2$) state, the equation changes to:

$$(\mu_{eff}/\mu_B)^2 = 24(1/2+3/2X)+15(1-2X) = 27+6X \quad (2)$$

in which each μ_{eff}/μ_B value was calculated using $2\sqrt{S(S+1)}$ where S is the spin quantum number. If, however, Mn^{3+} ions are in the low-spin state ($S=1$), then:

$$(\mu_{eff}/\mu_B)^2 = 8(1/2+3/2X)+15(1-2X) = 19-18X \quad (3)$$

For the compositional range $0<X<1$, μ_{eff}^2 is given by:

$$(\mu_{eff}/\mu_B)^2 = X\mu^2_{Co^{2+}} + (1/2+1/2X)\mu^2_{Co^{3+}} + (1/2+1/2X)\mu^2_{Mn^{3+}} + (1-X)\mu^2_{Mn^{4+}} \quad (4)$$

where $\mu_{Co^{2+}}$ is the spin-only paramagnetic moment of high-spin Co^{2+} ($S=3/2$). In the case that Mn^{3+} is high-spin, then:

$$(\mu_{eff}/\mu_B)^2 = 15X+24(1/2+1/2X)+15(1-X) = 27+12X \quad (5)$$

and for low-spin Mn^{3+}:

$$(\mu_{eff}/\mu_B)^2 = 15X+8(1/2+1/2X)+15(1-X) = 19+4X \quad (6)$$

Eqns. (2), (3), (5) and (6) are plotted together with observed $(\mu_{eff}/\mu_B)^2$ data in Fig. 8. Except for the data point at $X=0.597$, the observed curve can be explained by the co-existence of low-spin and high-spin Mn^{3+} when the Mn valence state (n) is larger than 3.5. The compositional dependence of the paramagnetic moment is similar to that for $Li_{1+X}Mn_{2-X}O_4$: $0<X<0.33$ (*i.e.* a solid solution between $LiMn_2O_4$ and $Li_4Mn_5O_{12}$);[38] observed μ_{eff} values above $n=3.6$ were smaller than calculated from a combination of high-spin Mn^{3+} and Mn^{4+}. The similarity of μ_{eff}–X plots between $Li_4Mn_5O_{12}$–Co_2MnO_4 and $LiMn_2O_4$–$Li_4Mn_5O_{12}$ solid solutions indicates that the compositional dependence of paramagnetic moment originates mainly from the mixed valence state of Mn^{3+} and Mn^{4+} in octahedral 16d sites. The reason for the occurrence of low-spin Mn^{3+} ions is still unclear. One factor that may contribute to this is the strength of the ligand field around Mn^{3+} which increases with decreasing X due to the decrease in lattice parameter *a,* Fig. 2.

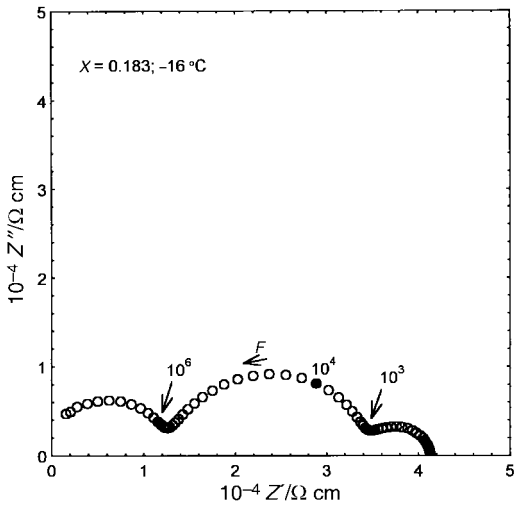

Fig. 9 Impedance data for composition $X=0.183$ at −16 °C.

Electrical conductivity

Impedance complex plane plots of data recorded on sintered pellets typically showed two or three arcs. Thus, for composition $X=0.183$, Fig. 9, the high frequency arc has an associated capacitance, calculated from the relation $\omega RC=1$ at the arc maximum, of 2.5×10^{-12} F, typical of a bulk response.[34] The middle frequency arc, with an associated capacitance of 3.6×10^{-10} F, corresponds to a grain boundary resistance.[34] The low frequency arc with capacitance 1.3×10^{-7} F may be ascribed to Schottky barrier phenomena[39] at the sample–electrode interface. For $X=1$ (not shown), two partly-resolved arcs are seen with capacitances 5.8×10^{-12} F, corresponding to the bulk response, and 3.9×10^{-11} F, corresponding to the grain boundary response. A low frequency response attributable to Schottky barrier phenomena exists, but is almost hidden by the large grain boundary response.

Resistance values for the various components were obtained from the arc diameters, or their intercepts on the real, Z' axis. The grain boundary resistance was 2–3 times larger than the bulk resistance in the range $-0.173 \leqslant X<1$, but was *ca.* 10 times larger than the bulk resistance for $X=1$. However, the

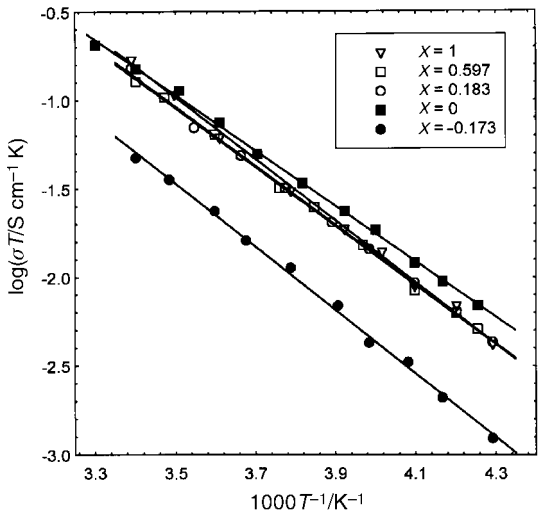

Fig. 10 Conductivity Arrhenius plots for spinel solid solutions.

grain boundary capacitance for $X=1$ was *ca.* 10 times smaller than that for $-0.173 \leqslant X < 1$ which implies that the grain boundary thickness in the former case is *ca.* 10 times greater than that in the latter. The grain boundary impedance may represent the formation of an impurity phase or a segregation effect but, given the variation in its capacitance, it may also correspond to a constriction resistance associated with incomplete densification of the pellets during sintering, especially for composition $X=1$. As commented above, the stoichiometry and structure of 'Co_2MnO_4' is not fully resolved and similarly, its electrical conductivity data show complexity and require further investigation.

No low-frequency spikes attributable to a blocking electrode response, Fig. 9, were seen in the measured temperature and frequency ranges throughout the compositional range $-0.173 \leqslant X \leqslant 1$, and thus, as expected, the main conductive species is likely to be electrons.

All the present samples show similar bulk conductivities at room temperature, in the range 2.0×10^{-4} to 6.3×10^{-4} S cm^{-1}, consistent with a modest level of semiconductivity, Table 4. This may be attributed to the presence of neighbouring Mn^{3+}/Mn^{4+} ions in octahedral sites.[40] Bulk conductivities, σ, fit the Arrhenius equation, $\sigma(T)=\sigma_0 \exp(-\Delta H/kT)$, where σ_0 is the pre-exponential factor, ΔH activation energy, and k Boltzmann's constant, Fig. 10. All the samples exhibit low ΔH, 0.31 to 0.36 eV, which shows a minimum at $X=0$ and increases slightly to either side, Table 4. The lattice parameter, a, also passes through a minimum at $X=0$, Fig. 2, which leads to the conclusion that ΔH increases with a and hence with the distance for electron hopping. The compensation rule appears to apply to this solid solution: an increase in ΔH accompanies an increase in σ_0 which acts to suppress any change in conductivity, Table 4.

Electrochemical properties

Charge–discharge experiments were carried out to extract lithium reversibly from the solid solutions, using electrochemical cells, Li/$LiPF_6$, propylene carbonate/$Li_{2-2X}Co_{1+3X}Mn_{3-X}O_8$. Fig. 11 shows potential profiles of a selection of cells during the first cycle. For $-0.173 \leqslant X \leqslant 0.183$, two reversible plateaux centred on *ca.* 4.0V and *ca.* 5.1V are seen; for $X=0.381$, only one reversible plateau, centred on *ca.* 4.0 V, is seen and for $0.60 \leqslant X \leqslant 1$ both plateaux disappear.

Table 4 Conductivity Arrhenius parameters for spinel solid solutions $Li_{2-2X}Co_{1+3X}Mn_{3-X}O_8$

X	ΔH/eV	$\log_{10}[\sigma_0$/S cm$^{-1}]$	$\sigma_{25\,^\circ C} \times 10^4$/S cm^{-1}
−0.173	0.355	4.79	2.06
0	0.311	4.51	6.04
0.183	0.332	4.81	5.38
0.597	0.331	4.79	5.27
1	0.346	5.12	6.25

Co_2MnO_4 ($X=1$) contains no Li to extract, but a cell with it as the cathode shows irreversible, false charge capacity of *ca.* 7 mA h g^{-1}, which is probably caused by electrolyte oxidation above *ca.* 5.0 V, Fig. 11. Such false charge capacity arose for all cells, as seen from a constant difference between total discharge and subsequent total charge capacities upon cycling for one composition, $X=-0.173$, in Fig. 12, and ranged from 4 to 8 mA h g^{-1}, depending on X. [Note: for compositions $X<0$, the difference between charge and discharge capacities was considerably greater in the early cycles; this is discussed later.] In the following, the capacity data have been corrected for false charge capacity.

The theoretical total capacity, defined as the capacity obtainable after complete extraction of lithium from $Li_{1-X}Co_{1/2+3X/2}Mn_{3/2-X/2}O_4$, decreases with X, Fig. 13. The total charge capacity on the first cycle is slightly smaller than the corresponding theoretical value in the range $0 \leqslant X \leqslant 0.183$, but the difference between the two increases for compositions outside this range. Also, the discharge capacity on the first cycle was often lower than on second and subsequent cycles, Fig. 12.

For most cells, in each cycle, the total discharge capacity was only slightly smaller than that in the previous cycle when the current density was fixed at 0.5 mA cm^{-2}, Fig. 12; thus, by the end of every discharge, the cathode material had regained almost all of the lithium extracted during the previous charge. Cells were typically tested for 36 cycles, by the end of which discharge capacities had decreased to 75–85% of their initial values, Fig. 12. The cells showed small drops in discharge capacity when higher current densities were used: 2.5 mA cm^{-2} for the 3rd–4th discharges, 5.0 mA cm^{-2} for the 5th–6th discharges, Fig. 12, and thus appeared to sustain cycling with current densities significantly higher than 0.5 mA cm^{-2}.

On initial charge, a cell with $Li_2CoMn_3O_8$ ($X=0$) exhibits a plateau centred on 4.0 V with the capacity, estimated at the sharp transition point to the second plateau centred on 5.2 V of 66.1 mA h g^{-1}, Fig. 11. On converting this capacity to Z in $Li_{2-Z}CoMn_3O_8$, Z reaches 0.90. After subtracting the false charge capacity caused by electrolytic oxidation, the initial charge plateau centred on 5.2 V has capacity 65.2 mA h g^{-1}, Fig. 14. This capacity is almost the same as that of the plateau centred on 4.0 V, and corresponds to a change in Z of 0.89. Initial discharge capacity is estimated to be *ca.* 62 mA h g^{-1} at the plateau centred on 5.1 V and *ca.* 69 mA h g^{-1} at the plateau centred on 4.0 V, Fig. 11. The plateaux at 4 and 5 V have been attributed previously[30] to the redox reactions, $Mn^{3+}{}_{16d} \leftrightarrow Mn^{4+}{}_{16d}$ and $Co^{3+}{}_{16d} \rightarrow Co^{4+}{}_{16d}$, respectively although confirmation of the oxidation states on charging is still needed. Since composition $X=0$ has equal amounts of Co^{3+} and Mn^{3+}, there appears to be a direct correlation between this and the similar lengths of the two plateaux.

For cells with $X \neq 0$, the electrochemical performance on initial charge–discharge was considerably more complex than for $X=0$, Fig. 11. First, the 4 V to 5 V transition on charging was generally sharp for compositions close to $X=0$ but the same transition on discharge, for the first and possibly second cycles, was very broad, especially for $X<0$. Second, the data sets for $X \geqslant 0$, on both charging and discharging showed a gradual increase in voltage over the 4.0 to 4.3 V range prior to the more rapid transition to the 5 V range. Third, there was much hysteresis between charging and discharging for $X<0$ which caused the plateau at 4 V to be longer on discharge than on charge; conversely the 5 V plateau on discharge was much shorter than on charge for these compositions. This effect was most noticeable for $X=-0.173$ but was observed only on the

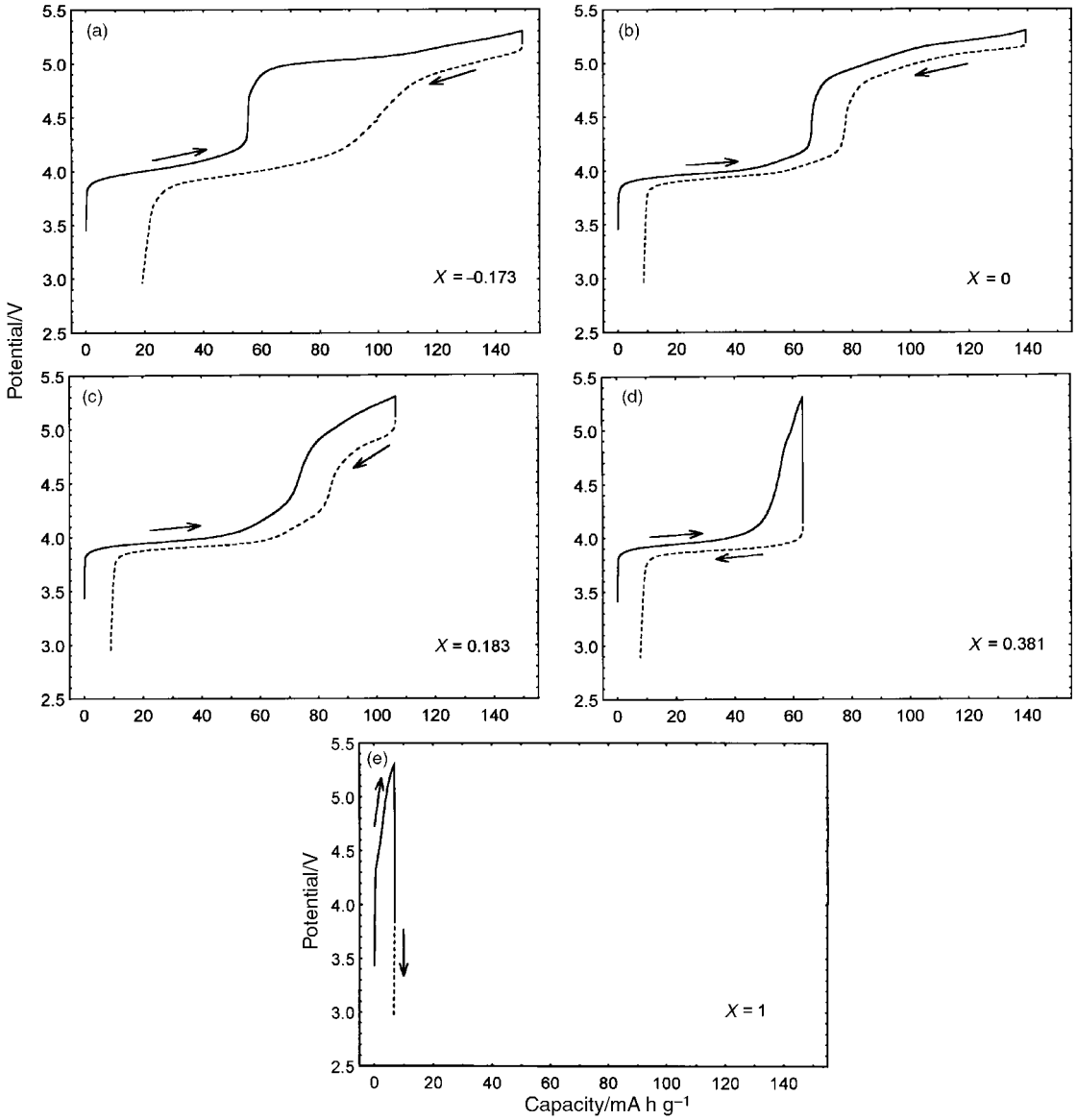

Fig. 11 Potential profiles for electrochemical cells, Li/$LiPF_6$, propylene carbonate/$Li_{2-2X}Co_{1+3X}Mn_{3-X}O_8$: solid line, first charge; dotted line, first discharge.

first charge–discharge cycle; subsequent cycles had an appearance much more similar to that of other compositions.

The composition dependence of the sizes of the two plateaux on charge and discharge is shown in Fig. 14. The 5 V discharge passes through a maximum at $X=0$, whereas the 4 V discharge passes through a minimum at $X=0$. These two effects largely cancel in the total discharge capacity which is almost constant for $X \leqslant 0$, before decreasing for $X>0$.

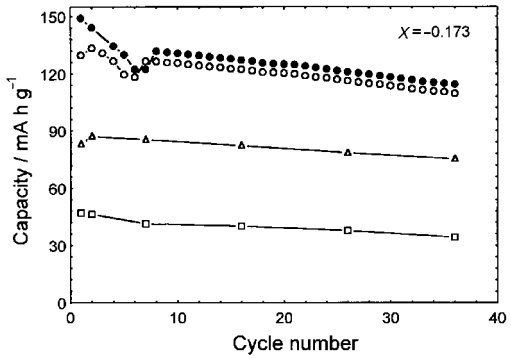

Fig. 12 Variation in total charge (●) and discharge (○) capacity and discharge capacity of the plateaux centred on *ca.* 4.0 V (Δ) and *ca.* 5.1 V (□) upon cycling, for electrochemical cells, Li/$LiPF_6$, propylene carbonate/$Li_{1-X}Co_{1/2+3X/2}Mn_{3/2-X/2}O_4$: ○ = Δ + □. The dip in the data points for the 5th and 6th discharges and subsequent recharges is associated with the use of higher discharge current densities.

Discussion

For $X=0$, we note that: (1) all Li^+ is situated in tetrahedral 8*a* sites with full occupancy, and can thus move smoothly through the well-known tetrahedral 8*a* site–empty octahedral 16*c* site pathway;[14,26] (2) reasonably good electronic transport occurs; (3) oxidation of Co^{3+} and Mn^{3+} in octahedral sites is certainly feasible. Therefore, full extraction of lithium from $X=0$ may in principle occur, yielding a plausible end formula, $[Co^{4+}{}_{0.5}Mn^{4+}{}_{1.5}]_{16d}O_4$. In practice, the cathode composition after the first charge to 5.3 V was estimated to be $Li_{0.21}CoMn_3O_8$, indicating that the positive electrode still contained *ca.* 10% Li, which could probably be extracted at higher potentials if the electrolyte used were chemically and electrochemically stable.

Two redox reactions appear to take place in $Li_2CoMn_3O_8$ on cycling: (1) $Mn^{3+}{}_{16d} \leftrightarrow Mn^{4+}{}_{16d}$; (2) $Co^{3+}{}_{16d} \leftrightarrow Co^{4+}{}_{16d}$. A plateau centred on *ca.* 4.0 V has been attributed to reaction (1) for several cells with spinel cathodes including $LiMn_2O_4$,[1]

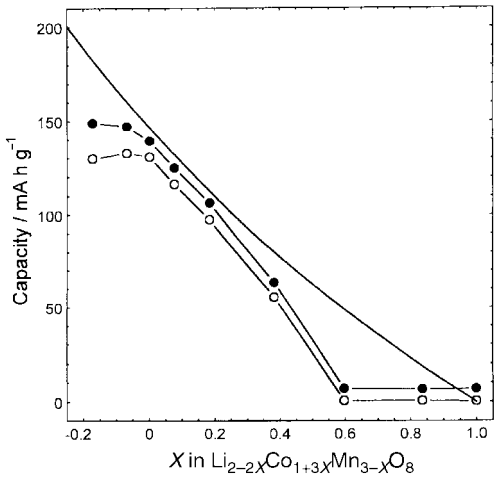

Fig. 13 Variation in initial total charge, uncorrected for false capacity caused by electrolyte oxidation (●) and discharge (○) capacity with composition, X, for electrochemical cells, Li/$LiPF_6$, propylene carbonate/$Li_{2-2X}Co_{1+3X}Mn_{3-X}O_8$. The theoretical total capacity (solid line) is the capacity obtainable by the full extraction of lithium from $Li_{2-2X}Co_{1+3X}Mn_{3-X}O_8$.

$Li_2CrMn_3O_8$,[16] $Li_2NiMn_3O_8$ [19] and $Li_2CuMn_3O_8$.[22] It is thus possible that reaction (2) is responsible for the plateau centred on 5.1 V and indeed, this has been indicated by systematic investigation of electrochemical properties for the spinel solid solutions $Li_2Co_{1+Y}Mn_{3-Y}O_8$.[30]

When $X>0$, Co that resides in tetrahedral 8*a* sites blocks Li^+ conduction through the tetrahedral site–empty octahedral site pathway, and thus impedes the extraction of Li from the solid solutions. The degree of channel blocking by Co increases with X,[26] Fig. 5, and appears to be responsible for the increasing difference between total charge/discharge capacities and the corresponding theoretical total capacity; thus, when $X\geqslant 0.6$, channel blocking by Co appears to be large enough for the solid solutions to lose their electrochemical activity as the cathode, Fig. 13.

When $X<0$, the concentration of Li in octahedral 16*d* sites increases with decreasing X; it may be difficult to extract Li from and reinsert Li into these octahedral sites since there appear to be no facile conduction pathways for them. This could account for the observation that the total discharge capacities are essentially constant for $X\leqslant 0$ if it is assumed that

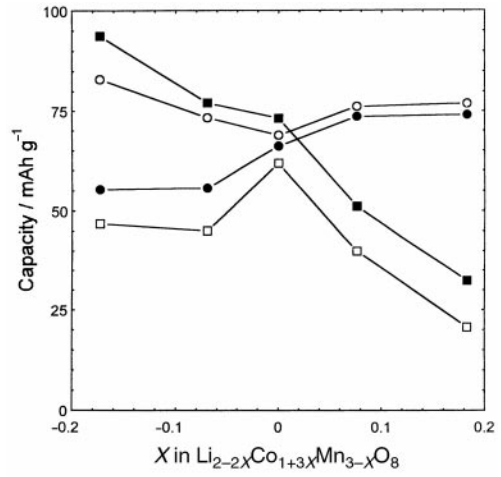

Fig. 14 Variation with composition, X, in initial charge (uncorrected) and discharge capacity of the plateaux centred on *ca.* 4.0 V (●/○) and *ca.* 5.1 V (■/□), for electrochemical cells, Li/$LiPF_6$, propylene carbonate/$Li_{2-2X}Co_{1+3X}Mn_{3-X}O_8$: ● + ■ = initial total charge capacity uncorrected for false capacity caused by electrolyte oxidation; ○ + □ = initial total discharge capacity.

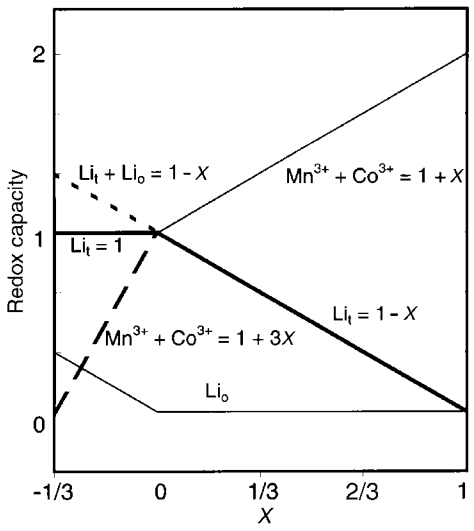

Fig. 15 Composition dependence of theoretical capacity for different redox-active processes.

only Li in tetrahedral sites is electrochemically active and since the tetrahedral sites are fully occupied by Li, Fig. 5, for $X\leqslant 0$. With decreasing X in this range, the amount of Co^{3+} present decreases, Fig. 5 [the Co content is $\frac{1}{2}+3X/2$; for instance, for $X=-0.173$ the Co content is 0.24 compared to 0.50 for $X=0$] and therefore, the decreasing size of the 5 V discharge plateau with decreasing X may correlate directly with the Co content. This does not explain, however, why the 5 V plateau on initial charging should *increase* with decreasing X, Fig. 14; there is insufficient Co present to account for the values observed and therefore, in this region on initial charging, a second factor must contribute to the 5 V plateau.

Additional difficulties arise in trying to correlate the size of the 4 V plateau with the Mn^{3+} content, especially at low X. From the general formula of the solid solutions, the Mn^{3+} and Co^{3+} contents are equal for all X and increase with X, Fig. 5. For $X<0$, there is insufficient Mn^{3+} to account for the size of the 4 V plateau, especially on discharge. Considering the total discharge capacity, there is insufficient Co^{3+} and Mn^{3+}, combined, to account for the relatively large values obtained at low X, especially for composition $X=-0.173$. This is shown schematically in Fig. 15. Theoretical capacity can be defined in three ways. First, if the theoretical capacity is related to the sum of the Mn^{3+} and Co^{3+} contents, its value decreases to zero at $X=-1/3$. Second, if the theoretical capacity is proportional to the Li content in tetrahedral sites, then this should be constant over the range $-0.33<X<0$ (thick continuous line). Third, if the theoretical capacity is related to the total Li content, then this should increase at negative values of X (thick dotted line). The first definition is the one that is conventionally adopted, in which it is assumed that the final charged states of both Co and Mn are 4+. The experimental data, Fig. 13, fit most closely to the second definition of theoretical capacity, however, demonstrating the need for an additional redox process.

In order to explain the results for $X<0$, we are therefore forced to consider alternative redox couples. There are two possibilities, $Mn^{4+}\leftrightarrow Mn^{5+}$ and $O^{2-}\leftrightarrow O^-$; at this stage we make no attempt to distinguish between them but do note that the possible role of oxygen as a redox-active species in other systems has been proposed.[41] The large hysteresis observed for charging/discharging of compositions with $X<0$, together with the significant difference in charge and discharge capacities during the first cycle, may be related to the occurrence of an additional redox process. Possibly also, an irreversible process occurs during the first charge; this could be loss of some O_2 gas if oxide ions are fully oxidised; or some reorganisation within

the spinel structure may occur. At this stage, we cannot comment further on any possible changes.

The spinel solid solutions of general formulae $Li_{1-X}Co_{1/2+3X/2}Mn_{3/2-X/2}O_4$ and $Li_1Co_{1/2+Y/2}Mn_{3/2-Y/2}O_4$,[30] Fig. 1, are now known to constitute a large family of 5 V lithium cathode materials. One of the most promising compositions as a cathode in practical 5 V lithium batteries is $LiCoMnO_4$ ($Y=1$),[23,30] which would in principle, have the capacity of *ca.* 145 mA h g^{-1} at a long plateau centred on *ca.* 5.1 V and thus an energy density of *ca.* 740 W h kg^{-1}, provided that $LiCoMnO_4$ with the formula $[Li^+]_{8a}[Co^{3+}Mn^{4+}]_{16d}O_4$ is used in contact with an electrolyte that is chemically and electrochemically stable to *ca.* 5.5 V.[14,30] This family of 5 V lithium cathode materials is likely to extend further within the spinel solid solution domain in the system Li–Co–Mn–O, and some of these compositions may exhibit superior performance to $LiCoMnO_4$ as a lithium battery cathode.

Acknowledgements

HK thanks CVCP for an ORS Award.

References

1 See, for example, R. Koksbang, J. Barker, H. Shi and M. Y. Saidi, *Solid State Ionics*, 1996, **84**, 1; P. G. Bruce, *Chem. Commun.*, 1997, 1817.
2 T. Nagaura and K. Tozawa, *Prog. Batteries Sol. Cells*, 1990, **9**, 209.
3 Japan Electronics, March 6th, 1996.
4 K. Mizushima, P. C. Jones, P. C. Wiseman and J. B. Goodenough, *Mater. Res. Bull.*, 1980, **15**, 783.
5 T. Ohzuku, M. Kitagawa and T. Hirai, *J. Electrochem. Soc.*, 1990, **137**, 769.
6 J.-M. Tarascon, E. Wang, F. K. Shokoohi, W. R. McKinnon and S. Colson, *J. Electrochem. Soc.*, 1991, **138**, 2859.
7 A. Yamada, K. Miura, K. Hinokuma and M. Tanaka, *J. Electrochem. Soc.*, 1995, **142**, 2149.
8 *JEC Battery Newsletter*, Sony Corporation Battery Group and Sony Energytec, July–August, 1993, p. 19.
9 A. R. Armstrong and P. G. Bruce, *Nature*, 1996, **381**, 499.
10 P. G. Bruce, A. R. Armstrong and H. Huang, *J. Power Sources*, 1997, **68**, 19.
11 J. Kim and A. Manthiram, *Nature*, 1997, **390**, 265.
12 J.-M. Tarascon and D. Guyomard, *Solid State Ionics*, 1994, **69**, 293.
13 D. Guyomard and J.-M. Tarascon, *J. Power Sources*, 1995, **54**, 92.
14 H. Kawai, M. Nagata, H. Tukamoto and A. R. West, *J. Power Sources*, 1999, **81–82**, 67.
15 C. Sigala, D. Guyomard, A. Verbaere, Y. Piffard and M. Tournoux, *Solid State Ionics*, 1995, **81**, 167.
16 C. Sigala, A. Verbaere, J. L. Mansot, D. Guyomard, Y. Piffard and M. Tournoux, *J. Solid State Chem.*, 1997, **132**, 372.
17 H. Kawai, M. Nagata, M. Tabuchi, H. Tukamoto and A. R. West, *Chem. Mater.*, 1998, **10**, 3266.
18 H. Kawai, M. Nagata, H. Tukamoto and A. R. West, *J. Mater. Chem.*, 1998, **8**, 837.
19 Q. Zhong, A. Bonakdarpour, M. Zhang, Y. Gao and J. R. Dahn, *J. Electrochem. Soc.*, 1997, **144**, 205.
20 K. Amine, H. Tukamoto, H. Yasuda and Y. Fujita, *J. Power Sources*, 1997, **68**, 604.
21 Y. Ein-Eli and W. F. Howard Jr., *J. Electrochem. Soc.*, 1997, **144**, L205.
22 Y. Ein-Eli, W. F. Howard Jr., S. H. Lu, S. Mukerjee, J. McBreen, J. T. Vaughey and M. M. Thackeray, *J. Electrochem. Soc.*, 1998, **145**, 1238.
23 H. Kawai, M. Nagata, H. Tukamoto and A. R. West, *Electrochem. Solid State Lett.*, 1998, **1**, 212.
24 G. T-K. Fey, W. Li and J. R. Dahn, *J. Electrochem. Soc.*, 1994, **141**, 2279.
25 V. S. Hernandez, L. M. T. Martinez, G. C. Mather and A. R. West, *J. Mater. Chem.*, 1996, **6**, 1533.
26 H. Kawai, M. Tabuchi, M. Nagata, H. Tukamoto and A. R. West, *J. Mater. Chem.*, 1998, **8**, 1273.
27 M. A. Lafontaine, M. Leblanc and G. Ferey, *Acta Crystallogr., Sect. C*, 1989, **45**, 1205.
28 S. J. Martin, M. O'Keeffe and D. E. Partin, *J. Solid State Chem.*, 1994, **113**, 413.
29 R. J. Gummow, D. C. Liles, M. M. Thackeray and W. I. F. David, *Mater. Res. Bull.*, 1993, **28**, 1177.
30 H. Kawai, M. Nagata, H. Kageyama, H. Tukamoto and A. R. West, *Electrochim. Acta*, 1999, **45**, 315.
31 T. Takada, E. Akiba, F. Izumi and B. C. Chakoumakos, *J. Solid State Chem.*, 1997, **130**, 74.
32 B. Ammundsen, D. J. Jones, J. Roziere and G. R. Burns, *Chem. Mater.*, 1996, **8**, 2799.
33 B. Boucher, R. Buhl, R. di Bella and M. Perrin, *J. Phys. (Paris)*, 1970, **31**, 113.
34 I. M. Hodge, M. D. Ingram and A. R. West, *J. Electroanal. Chem.*, 1976, **74**, 125.
35 H. Rossouw, A. de Kock, L. A. Picciotto, M. M. Thackeray, W. I. F. David and R. M. Ibberson, *Mater. Res. Bull.*, 1990, **25**, 173.
36 M. Rietveld, *J. Appl. Crystallogr.*, 1969, **2**, 65.
37 S. McClure, *J. Phys. Chem. Solids*, 1957, **3**, 311.
38 C. Masquelier, M. Tabuchi, K. Ado, R. Kanno, Y. Kobayashi, Y. Maki, O. Nakamura and J. B. Goodenough, *J. Solid State Chem.*, 1996, **123**, 255.
39 See, for example, H. H. Sumathipala, M. A. K. L. Dissanayake and A. R. West, *J. Electrochem. Soc.*, 1995, **142**, 2138.
40 J. W. Verwey, P. B. Braun, E. W. Gorter, F. C. Romeijn and J. H. van Santen, *Z. Phys. Chem.*, 1951, **198**, 6.
41 G. Ceder, Y.-M. Chiang, D. R. Sadoway, M. K. Aydinol, Y.-L. Jang and B. Huang, *Nature*, 1998, **392**, 694.